Mon. Not. R. Astron. Soc. **378,** 416–428 (2007) doi:10.1111/j.1365-2966.2007.11811.x

# VIMOS-VLT spectroscopy of the giant Ly$\alpha$ nebulae associated with three $z \sim 2.5$ radio galaxies$^\star$

M. Villar-Martín,[1]† S. F. Sánchez,[2] A. Humphrey,[3] M. Dijkstra,[4]
S. di Serego Alighieri,[5] C. De Breuck[6] and R. González Delgado[1]

[1]*Instituto de Astrofísica de Andalucía (CSIC), Aptdo. 3004, 18080 Granada, Spain*
[2]*Centro Astronómico Hispano Aleman de Calar Alto (CSIC-MPIA), E4004 Almería, Spain*
[3]*Instituto de Astronomía, UNAM, Ap. 70-264, 04510 México, DF, México*
[4]*School of Physics, University of Melbourne, Parkville, Victoria, 3010, Australia*
[5]*INAF-Osservatorio Astrofisico di Arcetri, Largo Enrico Fermi 5, I-50125 Firenze, Italy*
[6]*European Southern Observatory, Karl Schwarschild Str, 2, D-85748 Garching bei München, Germany*

Accepted 2007 March 30. Received 2007 March 29; in original form 2006 November 17

**ABSTRACT**

The morphological and spectroscopic properties of the giant (>60 kpc) Ly$\alpha$ nebulae associated with three radio galaxies at $z \sim 2.5$ (MRC 1558–003, 2025–218 and 0140–257) have been investigated using integral field spectroscopic data obtained with the Visible Multi-Object Spectrograph (VIMOS) on VLT.

The morphologies are varied. The nebula of one source has a centrally peaked, rounded appearance. In the other two objects, it consists of two spatial components. The three nebulae are aligned with the radio axis within $\lesssim 30^\circ$. The total Ly$\alpha$ luminosities are in the range $(0.3–3.4) \times 10^{44}$erg s$^{-1}$. The Ly$\alpha$ spectral profile shows strong variation through the nebulae, with full width at half-maximum (FWHM) values in the range ∼400–1500 km s$^{-1}$ and velocity shifts $V_{\rm offset} \sim 120–600$ km s$^{-1}$.

We present an infall model that can successfully explain the morphology, size, surface brightness distribution and the velocity field of the Ly$\alpha$ nebula associated with MRC 1558–003. It can also explain why Ly$\alpha$ is redshifted relative to other emission lines and the FWHM values of the non-resonant He II line. This adds further support to our previous conclusion that the *quiescent* giant nebulae associated with this and other high-redshift powerful radio galaxies are in infall. A problem for this model is the difficulty to reproduce the large Ly$\alpha$ FWHM values, which might be the consequence of a different mechanism.

We have discovered a giant (∼85 kpc) Ly$\alpha$ nebula associated with the radio galaxy MRC 0140–257 at $z = 2.64$. It shows strikingly relaxed kinematics (FWHM < 300 km s$^{-1}$ and $V_{\rm offset} \lesssim 120$ km s$^{-1}$), unique among high-$z$ ($\gtrsim$2) radio galaxies.

**Key words:** galaxies: active – galaxies: high-redshift – galaxies: individual: MRC 1558–003 – galaxies: individual: MRC 2025–218 – galaxies: individual: MRC 0140–257.

## 1 INTRODUCTION

Powerful high-$z$ radio galaxies (HzRG; $z \gtrsim 2$) are often surrounded by giant Ly$\alpha$ nebulae which can extend for more than 100 kpc (e.g. McCarthy et al. 1990a; Reuland et al. 2003; Villar-Martín et al. 2003) and sometimes beyond the radio structures (e.g. Eales et al. 1993; Kurk et al. 2002; Maxfield et al. 2002). These are clumpy, irregular (with features such as filaments, plumes, ionization cones; e.g. Reuland et al. 2003) and often aligned with the radio axis (McCarthy, Spinrad & van Breugel 1995). They are characterized by extreme kinematics, with measured full width at half-maximum (FWHM) $\gtrsim$1000 km s$^{-1}$ (e.g. McCarthy, Baum & Spinrad 1996a; Villar-Martín et al. 2003), compared with values of a few hundred in low-redshift radio galaxies (e.g. Tadhunter, Fosbury & Quinn 1989; Baum, Heckman & van Breugel 1990). There is strong evidence that interactions between the radio structures and the ambient gas produce an outflow responsible for such extreme kinematics (van Ojik et al. 1997; Humphrey et al. 2006).

The nebulae have typical values of ionized gas mass $\sim 10^{9-10}$ M$_\odot$, Ly$\alpha$ luminosities ∼ several $\times 10^{43-44}$erg s$^{-1}$ and densities $n_e \sim$ a few to several hundred cm$^{-3}$ (e.g. McCarthy 1993; Villar-Martín et al.

$^\star$Based on observations carried out at the European Southern Observatory, Paranal (Chile). Programs 075.B-0212(A) and 073.B-0189(A).

†E-mail: montse@iaa.es

2003). They emit a rich emission-line spectrum dominated in the optical [ultraviolet (UV) rest frame] by Ly$\alpha$ followed by C IV$\lambda$1550, He II$\lambda$1640 and C III]$\lambda$1909 (hereafter C IV, He II and C III). Such a line spectrum reveals high levels of metal enrichment and excitation mechanisms mostly related to the nuclear activity, at least in the direction along the radio structures (e.g. Vernet et al. 2001).

In addition to the highly perturbed gas, HzRG are often embedded in giant (often $\geqslant$100 kpc), low surface brightness nebulae of metal-rich, ionized gas with *quiescent kinematics* (Villar-Martín et al. 2003; Reuland et al. 2007), i.e. not perturbed by interactions with the radio structures. We have recently shown that these quiescent nebulae are infalling towards the central region (Humphrey et al. 2007).

There are several narrow-band Ly$\alpha$ images of HzRG, and most spectroscopic studies have been performed with the long-slit technique, with the slit aligned with the radio structures. These studies have been seriously limited by, respectively, the lack of spectral information or the lack of spatial information in directions other than the radio axis. For this reason, we are carrying out an observational program of 3D integral field spectroscopy of powerful radio galaxies at $z \sim 2$–3 with the Visible Multi-Object Spectrograph (VIMOS) on VLT and the Potsdam Multi Aperture Spectrophotometer (PMAS) fibrebundle PPAK on the 3.5-m telescope in Calar Alto Observatory. The main goal is to characterize the morphological, kinematic and ionization properties of the extended ionized gas in two spatial dimensions.

In this paper, we present results obtained for MRC 1558–003 ($z = 2.53$), MRC 2025–218 ($z = 2.63$) and MRC 0140–257 ($z = 2.64$) based on VIMOS-VLT data. Results on MRC 2104–242 ($z = 2.49$) can be found in Villar-Martín et al. (2006). A similar study of 4C40.36 ($z = 2.27$) and 4C48.48 ($z = 2.34$) based on PMAS/PPAK data (3.5-m telescope, Calar Alto Observatory) will be presented in Sánchez et al. (in preparation).

A $\Omega_\Lambda = 0.73$, $\Omega_m = 0.27$ and $H_0 = 62\,\mathrm{km\,s^{-1}Mpc^{-1}}$ cosmology is adopted in this paper (Sánchez 2006).

## 2 OBSERVATIONS AND DATA REDUCTION

The observations [program 075.B-0212(A)] were made on UT 2005 July 28, 29 and 30 using the VIMOS (Le Févre et al. 2003) on the Nasmyth focus of the VLT Unit Telescope 3 (UT3). The instrument is equipped with an integral field unit with 6400 microlenses coupled to fibres. For the configuration selected by us, the number of fibres in use is 1600, covering $27 \times 27$ arcsec$^2$ on the sky with a 0.67 arcsec sampling. The $HR_{blue}$ grating was used with an effective wavelength range $\sim$4150–6200 Å, an instrumental profile of FWHM $1.7 \pm 0.2$ Å and a pixel scale of 0.5 Å pixel$^{-1}$.

The exposure time on each target was 7.3 h ($22 \times 1200$ s) on MRC 1558–003, 10 h ($30 \times 1200$ s) on MRC 2025–218 and 8.3 h ($25 \times 1200$ s) on MRC 0140–257. In addition, we had 4.5 h ($9 \times 1800$ s) on MRC 1558–003 obtained in 2004 June [program 073.B-0189(A); see Villar-Martín et al. 2006 for a description of these observations]. The total integration time on this source was therefore 11.8 h.

The seeing FWHM during the observations was in the range $\sim$0.44–1.32 arcsec (first night), 0.4–1.2 arcsec second night) and 0.5–3.0 arcsec (third night) for the 2005 observations, and 1.0–1.4 arcsec for the 2004 data on MRC 1558–003.

For each galaxy, a dithering pattern was applied with a maximum offset of $\sim$3 arcsec, and a range of dithering pointings between 3 and 7.

The data were reduced using R3D (Sánchez 2006) and IRAF routines. The data were bias subtracted. The locations of the spectra were traced on a continuum-lamp exposure obtained before each target exposure. The corresponding spectrum was then extracted for each fibre by co-adding the flux intensity within a 5-pixel aperture, along the spectral dispersion axis, centred on the estimated location of the fibre centroid.

The wavelength calibration was performed using arc lamp spectra and the telluric emission lines in the science data. The wavelength solution was stable within a fraction of 1 spectral pixel (0.5 Å) across the whole spectral range and the whole field of view (FOV).

The wavelength calibration in the blue (i.e. the Ly$\alpha$ spectral region) was problematic due to the lack of bright emission lines in the arc lamp and sky spectra. Residual, artificial shifts in $\lambda$ of up to 6 Å were measured for Ly$\alpha$ relative to C IV and He II in MRC 1558–003 and 2025–218. We have been able to correct for this effect by comparing with available Keck long-slit spectroscopy (Villar-Martín et al. 2003; Humphrey 2004) to an accuracy of $\lesssim$1 Å. In any case, such uncertainty will not affect the results presented here.

The fibre-to-fibre response at each wavelength was determined from a continuum-lamp exposure.

After these basic reduction steps, a data cube was created for each exposure. The cubes for MRC 2025–218 were then recentred spatially at each wavelength by determining the centroid of a nearby star in the VIMOS FOV. This recentring corrects for differential atmospheric refraction.

For the other two objects, there are no stars in the VIMOS FOV. We used the information on the spatial shifts contained in the image headers to apply the corresponding shifts. However, we found that this technique left substantial spatial offsets. For this reason, we used the Ly$\alpha$ peak of emission to recentre all cubes. Although this recentring is valid in the blue, it is not clear that it is also valid in the red. In particular, in the case of MRC 1558–003, we found a residual spatial shift of $\sim$1 spaxel in the direction of the radio structures between the blue (Ly$\alpha$) and red (C IV, He II) parts of the spectrum, which is much larger than found in previous works (Villar-Martín et al. 1999; Humphrey et al. 2007). For this reason, an additional correction was applied. Uncertainties remain regarding the spatial centring in the direction perpendicular to the radio axis, although this is likely to be $<$1 spaxel or 0.67 arcsec. This will not seriously affect the results presented here.

For MRC 0140–257, no useful previous works or additional data were available. Although the accuracy of the spatial centring between the red and the blue ends of the spectrum is uncertain, this will not affect the results presented here due to the nature of our analysis and the clear separation between the spatial components of the Ly$\alpha$ nebula.

The cubes were then combined using IRAF tasks, masking the broken and/or low-sensitivity fibres. A $3\sigma$ clipping algorithm removed cosmic rays. The sky background was estimated before subtraction by selecting the spectra of object-free areas and creating an interpolated data cube (using E3D; Sánchez 2004). A spatial median smoothing using a $4 \times 4$ spaxel box was applied.

The nights were non-photometric. Observations of standard stars were used to perform a relative calibration from blue to red. The absolute flux calibration for MRC 1558–003 and 2025–218 was done using available Keck long-slit spectroscopy along the radio axis. We extracted a pseudo-slit from the VIMOS data as similar as possible to the slit aperture of the Keck spectra. The flux in different spectral windows was then compared and scaled. The final flux calibration has an accuracy of $\sim$20 per cent. For MRC 0140–257, this could not be done due to the unavailability of a high-quality long-slit spectrum, but as we explain in Section 5.3, the agreement

between the measured Ly$\alpha$ flux and published values is reasonably good ($\sim$20 per cent).

Cross-talk effects are estimated to be negligible. The fibre-to-fibre contamination is expected to be <5 per cent for adjacent spectra in the CCD, dropping to less than 1 per cent for the third adjacent spectra.

To overlay the radio maps (Carilli et al. 1997; Pentericci et al. 2000) on the Ly$\alpha$ images, a different method was used for each object depending on the information available in the data. For MRC 2025–218, we placed the radio core at the position of the continuum centroid in the VIMOS data. Since this is a broad-line object (Section 3.2), it is reasonable to expect that this marks the location of the active galactic nucleus (AGN). This is further supported by the fact that the UV continuum has a spatially unresolved component (Section 3.2).

For MRC 1558–003, we positioned the radio core at the spaxel with the maximum Ly$\alpha$ flux, which is expected to be shifted by a few tenths of a spaxel relative to the continuum centroid (Humphrey et al. 2007). This method would be incorrect if the AGN is spatially shifted relative to the continuum and/or line centroids. However, we do not expect this to be the case since this is a broad-line object and, moreover, it shows little evidence for Ly$\alpha$ absorption (see below). The 1$\sigma$ uncertainty in the Ly$\alpha$-radio registration is $\sim$0.3 arcsec in both cases.

For MRC 0140–257, we assumed that the radio core is placed between the two Ly$\alpha$ spatial components, although it is not necessarily the case. This is the main source of uncertainty since the radio core could be shifted by 2 arcsec if it is associated with one of the two Ly$\alpha$ blobs (Section 4.3). The impact of this assumption on the interpretation of our results will be discussed when relevant.

### 2.1 VIMOS sensitivity

The main scientific goal of our VIMOS-VLT observational program is to study the properties of the giant nebulae associated with a sample of HzRG. By isolating spectroscopically and/or spatially, the emission from the perturbed and the quiescent gaseous components (e.g. Villar-Martín et al. 2003), one of our priorities is to characterize the morphological, kinematic and ionization properties of the quiescent gas. In this way, we can study the gas without the strong distortions that the radio structures can imprint on its observed properties. Such study has the potential to provide critical information on the star formation and chemical enrichment histories as well as the galaxy formation process (Villar-Martín et al. 2003; Humphrey et al. 2006, 2007).

In order to achieve these goals, it is critical to detect the main UV lines (especially Ly$\alpha$ and He II) with high signal-to-noise ratio (S/N) in the faint, outer regions of the objects, which are usually characterized by quiescent kinematics. Moreover, this would allow us to study in detail the high surface brightness regions (at least several times brighter). Although usually distorted by the radio structures, it should be possible to spectroscopically isolate the emission from the quiescent and the perturbed gas using especially the non-resonant He II line, as in Villar-Martín et al. (2003).

The faintest regions of our interest have often Ly$\alpha$ surface brightness levels which are, within the errors, consistent with or even below the detection limit or our VIMOS data ($3\sigma \sim 10^{-17}$ erg s$^{-1}$ cm$^{-2}$ arcsec$^{-2}$) for 8–10 h exposure time. For comparison, van Ojik et al. (1996) detected in 4 h the giant, quiescent, low surface brightness nebula ($\sim 10^{-17}$ erg s$^{-1}$ cm$^{-2}$ arcsec$^{-2}$) associated with a radio galaxy at $z = 3.6$ using long-slit spectroscopic data obtained with European Southern Observatory (ESO) Multi-Mode Instrument (EMMI) on the 3.5-m New Technology Telescope (NTT; La Silla). With a 2.5 arcsec wide slit, the spectral resolution was of 2.8 Å, not very different to that of our data. In the VIMOS data, not even Ly$\alpha$ could be definitively detected from the faintest regions of our interest, which at least in MRC 1558–003 and 2025–218 we knew exist (Section 3). He II and C IV are detected only from the highest surface brightness regions, but with not enough S/N to perform an adequate kinematic and ionization analysis in two spatial dimensions.

Thus, the investigation of the properties of the quiescent gas has been possible only for those objects where there is no signature of interactions between the radio structures and the gas (MRC 1558–003 and 0140–257; see Section 4) or objects with no spectroscopic blend between the perturbed and the quiescent nebula (MRC 2104–242; Villar-Martín et al. 2006). Moreover, in all three cases Ly$\alpha$ is not heavily absorbed. For objects where the emissions from the perturbed and the quiescent gas are blended (i.e. an important fraction of HzRG), a more sensitive instrument/telescope combination is needed.

## 3 PREVIOUS RESULTS

The three radio galaxies discussed in this paper, MRC 1558–003, 2025–218 and 0140–257, belong to the Molonglo Catalogue of high-redshift radio galaxies (Large et al. 1981; McCarthy et al. 1990b). The objects were selected based on previous evidence for strong Ly$\alpha$ emission. The two first objects were previously known to be associated with giant (>60 kpc) Ly$\alpha$ nebulae (see below).

### 3.1 MRC 1558–003 ($z = 2.53$)

This object is associated with radio structures which extend for $\sim$9 arcsec or 84 kpc (Pentericci et al. 2000) along a position angle (PA) of 75°.

Previous long-slit spectroscopic studies have shown that Ly$\alpha$ is extended for at least $\sim$14 arcsec ($\sim$130 kpc) along the slit with PA=72°, well beyond the radio structures (e.g. Villar-Martín et al. 2003). C IV and He II are extended across $\sim$6 arcsec, while N V, which is fainter, has a more compact appearance. The optical continuum is also extended.

ISAAC (Infrared Spectrometer and Array Camera) near-infrared spectroscopy revealed very broad H$\alpha$ (FWHM $\sim$ 11700 $\pm$ 900 km s$^{-1}$; Humphrey 2004; Humphrey et al., in preparation) evidence for an obscured broad-line region (BLR). According to the unified scheme of quasars and radio galaxies (Barthel 1989), the detection of BLR emission implies that the ionization cones axis is at a small angle to line of sight (LOS; <45°). This is further suggested by the detection of a clear one-sided radio jet (see Fig. 1).

High-resolution optical spectroscopy (FWHM $\sim$ 1.7 Å) showed no absorption features in the Ly$\alpha$ spectral profile integrated along PA = 85° (van Ojik et al. 1997). Absorption features were not found along PA = 75° by Villar-Martín et al. (2003), although the spectral resolution was rather low in this case (FWHM $\sim$11 Å). The small impact of absorption effects is also suggested by the large Ly$\alpha$/He II values measured across the nebula (Humphrey 2004; Villar-Martín et al. 2007)

For this object, no *Hubble Space Telescope* (*HST*) or emission-line images are available in the literature.

### 3.2 MRC 2025–218 ($z = 2.63$)

This radio galaxy is associated with a small radio source ($\sim$5 arcsec or 46 kpc; Carilli et al. 1997).

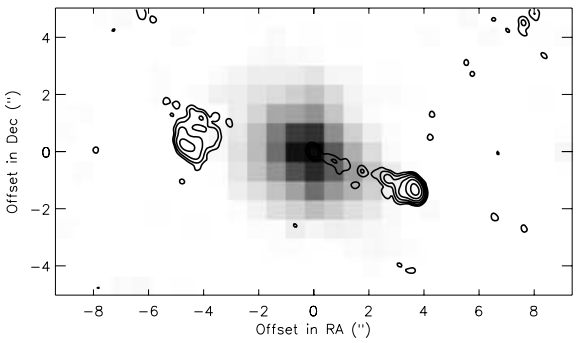


**Figure 1.** Lyα nebula (grey-scale) associated with MRC 1558–003 with the 8.2 GHz radio contours overlaid. The maximum extension of the nebula, as measured from the VIMOS data, is ∼9 × 7.5 arcsec$^2$ (84 × 70 kpc$^2$). The nebula is misaligned by ∼30 ± 5° relatively to the radio structures. North is up and East is towards left.

There is strong evidence for an obscured BLR in MRC 2025–218. The morphology of the object at optical and near-infrared wavelengths is dominated by a point source (Pentericci et al. 1999, 2001; McCarthy, Person & West 1992). Broad C IV and broad Hα (FWHM ∼ 6000 km s$^{-1}$) revealed by optical (Villar-Martín et al. 1999) and near-infrared (Larkin et al. 2000; Humphrey 2004; Humphrey et al., in preparation) spectra confirm this interpretation. The UV rest-frame continuum emission also shows an extended (∼6 arcsec) diffuse component, which is well aligned with the radio axis (Pentericci et al. 1999).

The Lyα emission is distributed bimodally (McCarthy et al. 1990b) north–south with two peaks that correspond roughly to the two radio lobes. The authors measured a total extension of ∼4 arcsec or 37 kpc. Keck long-slit optical spectroscopy (Humphrey 2004) reveals that Lyα is extended up to ∼9 arcsec or 83 kpc. C IV, He II and C III] are also spatially extended. C IV and C III] each have a spatially unresolved component centred at the continuum centroid and also an underlying extended component spanning ∼5 arcsec along the radio axis. NV is spatially unresolved.

Villar-Martín et al. (1999) detected absorption in the spectrum of MRC 2025–218 for C IV, C IIλ1335, Si IVλλ1393.8, 1402.8 and, maybe, O Iλ1302.2+ Si IIλ1402.8. The steep Lyα profile on the blue side of the line was also proposed to be a signature of absorption.

### 3.3 MRC 0140–257 ($z = 2.64$)

This object is associated with a small double radio source (4.2 arcsec or 39 kpc; Carilli et al. 1997). In the optical, it appears as a faint galaxy spatially extended and aligned with the radio source (McCarthy et al. 1992).

Lyα and Hα are the two lines detected in previous spectroscopic studies (McCarthy et al. 1991a; Eales & Rawlings 1996). It has not been reported whether the lines are spatially extended.

The F160W filter NICMOS-*HST* image (rest-frame spectral window 3850–4950 Å; Pentericci et al. 2001) shows two peaks of emission with almost the same flux (Pentericci et al. 1999), closely aligned with the radio axis. The authors suggest that this morphology could be due to a dust lane. There are a few fainter clumps within 2–3 arcsec.

Eales & Rawlings (1996) report Lyα/Hα = 0.31, which is ∼30 times lower than standard case B photoionization model predictions. As the authors explain, this value is very uncertain, since they had to assume a fixed value of the [N II]/Hα ratio (0.5), and no aperture corrections to the line fluxes were attempted. In spite of these uncertainties, the very large discrepancy with the model predictions suggests that Lyα absorption/extinction is present.

For this object, no emission-line images are available in the literature.

## 4 RESULTS

We present below the most relevant results obtained for the three radio galaxies investigated here.

### 4.1 MRC 1558–003 ($z = 2.53$)

*The Lyα nebula*

The VIMOS Lyα+continuum image of MRC 1558–003 was created by adding the monochromatic images of the object within the [4285–4315] Å range. A continuum image was subtracted to keep the line emission only. This was created by combining the images extracted from two adjacent spectral windows at both sides of Lyα, with the same spectral width as the line+continuum image. The resulting Lyα image is shown in Fig. 1 (see also Fig. 2), with the 8.2 GHz radio contours overlaid (Pentericci et al. 2000).

The nebula extends across ∼9 × 7.5 arcsec$^2$ or 84 × 70kpc$^2$. It is characterized by a strongly peaked rounded morphology. Emission from the nebula is detected only within the radio structures. The faintest Lyα emission we detect on the VIMOS image has surface brightness ∼10$^{-17}$ erg s$^{-1}$ cm$^{-2}$ arcsec$^{-2}$ (3σ values).

The angle between the nebular axis and the radio structures was measured using the PA on the sky of the longest dimension of the Lyα nebula and the PA of the line between the two brightest radio

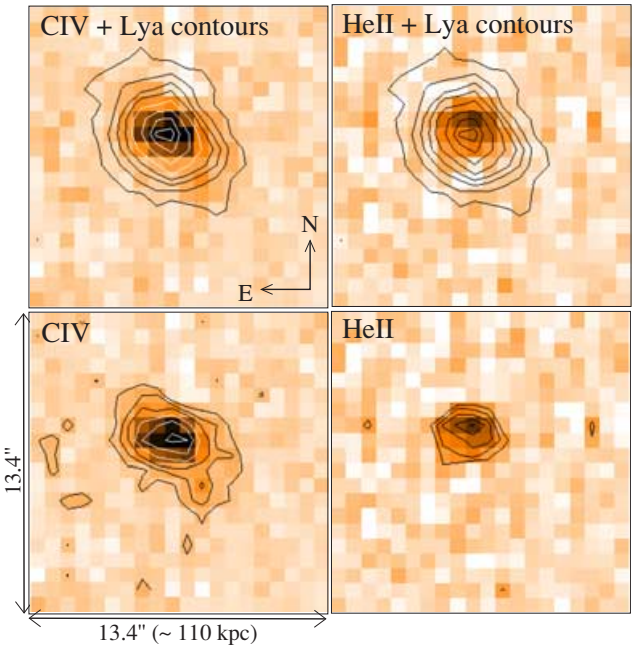


**Figure 2.** MRC 1558–003: comparison between the C IV, He II and Lyα spatial distributions (see electronic manuscript for the colour version for the figures). The underlying continuum has been subtracted from all images. Top panels: the Lyα morphology is shown with contours overlaid on the C IV (top left) and He II (top right) images (colour scale). The bottom panels show the C IV and He II morphologies. Lyα contours: (0.15, 0.6, 1.0, 1.6, 2.0, 3.2, 4.4, 4.4, 5.0) ×10$^{-16}$ erg s$^{-1}$ cm$^{-2}$ arcsec$^{-2}$; C IV contours: (1.8, 2.5, 4.1, 5.5, 7.0, 8.3) ×10$^{-17}$ erg s$^{-1}$ cm$^{-2}$ arcsec$^{-2}$; He II contours: (1.8, 2.4, 3.2, 3.9, 4.6, 5.3) ×10$^{-17}$ erg s$^{-1}$ cm$^{-2}$ arcsec$^{-2}$.

hotspots. The nebula is misaligned by $\sim 30 \pm 5^{\circ}$ relative to the radio axis.

As we found for MRC 2104–242 (Villar-Martín et al. 2006), Ly$\alpha$ emission is detected outside any plausible ionization cones with opening angle $\leqslant 90^{\circ}$ (Barthel 1989). Seeing effects are not likely to be responsible for this Ly$\alpha$ emission since the observations of this object were carried out under seeing conditions of FWHM $<$ 1.5 arcsec. Since this is a broad-line object, it is possible that the broad rounded morphology of the Ly$\alpha$ nebula is due to orientation effects (see Section 5.3). If the ionization cone axis lies close to the LOS, a broader, rounder morphology is expected.

The total Ly$\alpha$ flux integrated over the nebula is $4.8 \times 10^{-15}$ erg s$^{-1}$ cm$^{-2}$ corresponding to a luminosity of $3.4 \times 10^{44}$ erg s$^{-1}$.

### *C* IV *and He* II *morphologies*

The C IV and He II images were created by adding the monochromatic images of the object within the spectral windows [5455–5485] and [5780–5800] Å, respectively. Continuum images adjacent in wavelength to each line and of the same spectral width were subtracted to keep the line emission only.

The resulting images are shown in Fig. 2. The Ly$\alpha$ contours have been overplotted on the top panels for comparison. The C IV line is spatially extended with a maximum projected size of $\sim$7.5 arcsec. The outer, low surface brightness regions extend in the same direction as Ly$\alpha$. He II, which is fainter, appears more rounded and compact, although it is spatially resolved with a maximum extension of $\sim$3 arcsec.

The inner ($\sim$2 arcsec) regions of the C IV nebula seem to be extended along an axis (roughly E–W) which is shifted by $\sim 15^{\circ}$ anticlockwise relative to the axis defined by the outer regions and aligned within a few degrees with the radio structures. The He II emission seems to be extended also in this direction. There is some hint that this could also be the case for the inner Ly$\alpha$ nebula. However, higher spatial resolution data would be necessary to investigate whether there is a real rotation of the nebular axis as we move outwards, which could be a consequence of an inhomogeneous distribution of material.

Continuum is also detected, although the image is too noisy to characterize its morphology and determine its spatial centroid.

### *Spatially extended emission-line spectroscopy*

We show in Fig. 3 the spatial maps of the FWHM (corrected for instrumental profile) and velocity shift $V_{\rm offset}$ of the Ly$\alpha$ line. These values have been measured fitting Gaussian profiles spaxel to spaxel. $V_{\rm offset}$ has been computed relative to the Ly$\alpha$ emission at the spatial line centroid. The errors on the FWHM and $V_{\rm offset}$ are estimated to be, in general, $<$100 and $<$40 km s$^{-1}$, respectively.

Although the line profile is asymmetric at some spatial positions, this method allows a first-order study of the spatial variation of the Ly$\alpha$ spectral profile across the nebula. The line spectral profile shows strong spatial variations, as it is obvious from Fig. 3.

The first striking characteristic is that Ly$\alpha$ presents an increasing redshift towards the nebular centroid, with a maximum shift in velocity of $\sim$400 km s$^{-1}$ at this position relative to the outer regions.

The FWHM varies between $\sim$450 and 1350 km s$^{-1}$ across the nebula. Three distinct regions (*A*, *B* and *C* in Fig. 3) can be isolated in the FWHM map according to the linewidth. The maximum values are measured in region *B* (in the range 1050–1340 km s$^{-1}$), which runs approximately along the radio axis and contains the nebular centroid. The He II FWHM measured from the integrated spectrum is $600 \pm 100$ km s$^{-1}$. Region *A* shows narrower Ly$\alpha$, although the line is still quite broad (FWHM in the range 700–1030 km s$^{-1}$) while the He II FWHM is $650 \pm 200$ km s$^{-1}$ in the integrated spectrum. At some positions, He II is as narrow as $450 \pm 50$ km s$^{-1}$ (consistent with Villar-Martín et al. 2003). Ly$\alpha$ trends to be notably broader than He II (this was also found by Villar-Martín et al. 2003, along the radio axis).

Region *C* is clearly different both in linewidth [FWHM(Ly$\alpha$)) $=$ $650 \pm 50$ km s$^{-1}$; Fig. 4, bottom] and velocity shift. This region shows the largest blueshift relative to the Ly$\alpha$ centroid ($350 \pm 20$ km s$^{-1}$ for the integrated spectrum). C IV is detected in region *C*, although noisy, and it has FWHM $= 600 \pm 100$ km s$^{-1}$.

### *Ly$\alpha$ absorption*

We do not find definitive Ly$\alpha$ absorption features in the VIMOS data across the nebula. This is consistent with the previous studies (Section 3.1).

## 4.2 MRC 2025–218 ($z = 2.63$)

### *The Ly$\alpha$ nebula*

The VIMOS Ly$\alpha$+continuum image of MRC 2025–218 was created by adding the monochromatic images of the object within the [4385–4445] Å range. A continuum image extracted from an adjacent line-free region of the same spectral width was subtracted to keep the

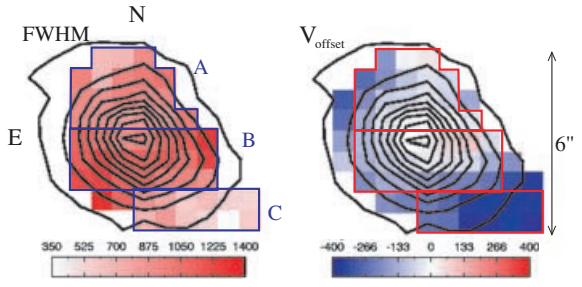


**Figure 3.** MRC 1558–003: Ly$\alpha$ spectral properties (see electronic version for colour figures). The FWHM (left-hand panel) (corrected for instrumental broadening) and the velocity shift (right-hand panel) relative to the line emission at the Ly$\alpha$ spatial centroid are shown. Values are in km s$^{-1}$. Ly$\alpha$ flux contours are overplotted. Regions *A*, *B* and *C* (see text) are identified. (Note that the spaxels, on which the FWHM and $V_{\rm offset}$ are determined, are not the same and depend on the S/N).

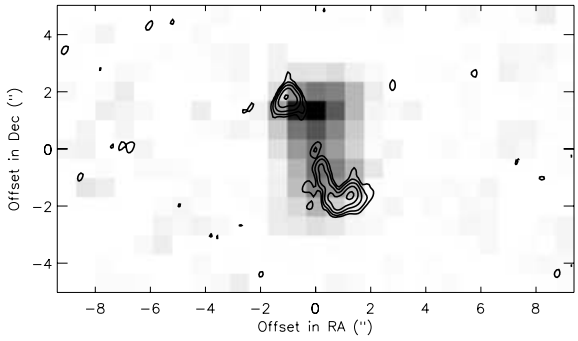


**Figure 4.** Ly$\alpha$ nebula (grey-scale) associated with MRC 2025–218 with 8.2 GHz radio contours overlaid. The maximum extension of the nebula as measured from the VIMOS data is $\sim$6 arcsec or 55 kpc. The nebula is similar in size to the radio source and is closely aligned with it (but see text). North is up and east towards left.

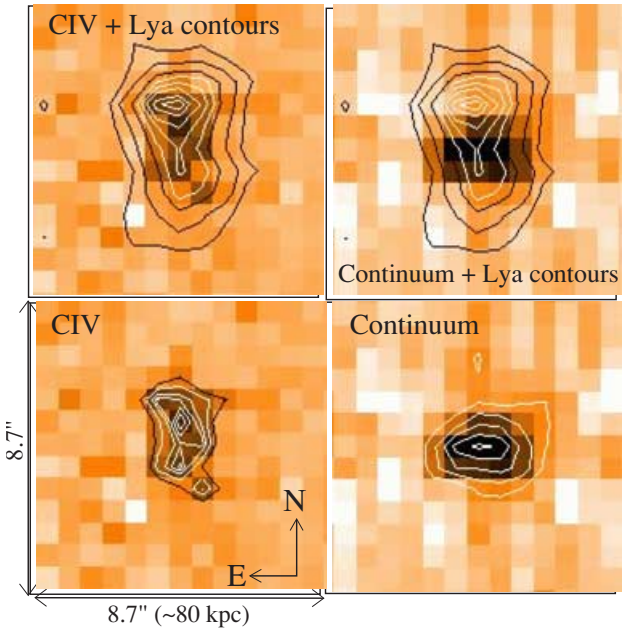


**Figure 5.** MRC 2025–218: comparison between the C IV, continuum and Ly$\alpha$ spatial distributions. Top panels: the Ly$\alpha$ morphology is shown with contours overlaid on the C IV (continuum subtracted, left-hand side) and continuum (right-hand side) images. Bottom panels: C IV (left-hand side) and continuum (right-hand side) images. C IV is extended in the same direction as Ly$\alpha$. The continuum centroid is located between the two Ly$\alpha$ spatial components, where the line flux presents a minimum. Ly$\alpha$ contours: (0.2, 0.5, 1.1, 1.4, 1.7, 2.1, 2.7, 3.0) $\times 10^{-16}$ erg s$^{-1}$ cm$^{-2}$ arcsec$^{-2}$. C IV contours: (1.4, 2.0, 2.5, 2.8, 3.2, 3.5) $\times 10^{-17}$ erg s$^{-1}$ cm$^{-2}$ arcsec$^{-2}$. Continuum contours: (1.7, 3.2, 4.5, 6.0, 7.5) $\times 10^{-16}$ erg s$^{-1}$ cm$^{-2}$ arcsec$^{-2}$.

line emission only. The resulting Ly$\alpha$ image is shown in Fig. 4, with the very large array (VLA) 8.2 GHz radio contours overlaid (Carilli et al. 1997, see also Fig. 5).

The Ly$\alpha$ maximum extension is ~6.0 arcsec or ~55 kpc, very similar to the radio source size. The faintest Ly$\alpha$ emission we detect on the VIMOS data has surface brightness $\sim 1.5 \times 10^{-17}$ erg s$^{-1}$ cm$^{-2}$ arcsec$^{-2}$ ($3\sigma$ values). The maximum extension in the direction perpendicular to the radio structures as measured from the VIMOS data is ~4 arcsec. As McCarthy et al. (1990b) already pointed out, the nebula is aligned with the radio structures within a few degrees. The bimodal distribution described in Section 3.2 is clearly seen.

The total Ly$\alpha$ flux integrated over the nebula is $2.1 \times 10^{-15}$ erg s$^{-1}$ cm$^{-2}$ corresponding to a luminosity of $1.7 \times 10^{44}$ erg s$^{-1}$.

### *C IV and continuum morphologies*

The C IV image (He II is too faint) was created by adding the monochromatic images of the object within the spectral window [5610–5650] Å and subtracting the adjacent continuum. The continuum image of the object was created by integrating across the [5670–5850] Å spectral window.

The resulting images are shown in Fig. 5. The Ly$\alpha$ contours have been overplotted (top panels) for comparison.

C IV extends for ~4 arcsec in the same direction as Ly$\alpha$ (N–S). The bimodal distribution shown by Ly$\alpha$ is distinguished in the C IV image. Interestingly, the continuum is spatially unresolved in this direction, but is barely resolved in the E–W direction, with a FWHM of $\sim 2.2 \pm 0.2$ arcsec, compared with FWHM $= 1.5 \pm 0.2$ arcsec for the star in the field. The continuum centroid is located between

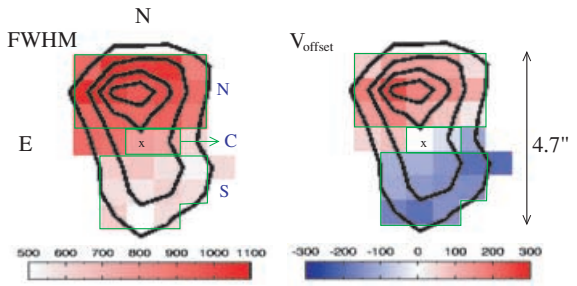


**Figure 6.** MRC 2025–218: Ly$\alpha$ spectral properties. The FWHM (left-hand side) (corrected for instrumental broadening) and the velocity shift (right-hand side) relative to the line emission at the continuum spatial centroid are shown. Values are in km s$^{-1}$. The location of the continuum centroid is shown with an 'x'. Ly$\alpha$ flux contours are overplotted. Regions *N*, *S* and *C* (continuum centroid) discussed in the text are overplotted.

the two Ly$\alpha$ spatial components, i.e., where this line presents a minimum.

### *Spatially extended emission-line spectroscopy*

We show in Fig. 6 the spatial maps of the FWHM and velocity shift $V_{\rm offset}$ of the Ly$\alpha$ line. As before, these values have been measured by fitting Gaussian profiles to the line spaxel by spaxel. $V_{\rm offset}$ has been computed relative to the Ly$\alpha$ emission at the position of the continuum centroid. The errors on the FWHM and $V_{\rm offset}$ are estimated to be, in general, <100 and <35 km s$^{-1}$, respectively.

This analysis reveals two clearly distinct regions (north and south), which are different both in FWHM and in $V_{\rm offset}$. These are coincident with the two Ly$\alpha$ spatial components discussed above. The continuum centroid (located between both regions) shows intermediate FWHM values. The Ly$\alpha$ spectra extracted from the Apertures *N* and *S* (north and south regions; Fig. 6) and the region in between (2 spaxels; see Aperture *C* in Fig. 6) are shown in Fig. 7 (left-hand panels). Both regions also emit C IV and He II (Fig. 7, top-right panel). The C IV–He II spectra (Fig. 7, top right panel) have been extracted using only the highest flux spaxels in the north and south regions (5 and 4 spaxels, respectively) in order to maximize the S/N for the lines. The differences in FWHM and $V_{\rm offset}$ seen in Fig. 6 are obvious also here.

The *S* region shows the narrowest Ly$\alpha$ spectral profiles (FWHM in the range 500–650 km s$^{-1}$) and the gas is blueshifted relative to the continuum centroid (values in the range $\sim -100$ to –200 km s$^{-1}$). C IV (which is a doublet and, therefore, expected to be intrinsically broader) and He II are also rather narrow, with FWHM $= 650 \pm 30$ and $500 \pm 30$ km s$^{-1}$, respectively, as measured from the spatially integrated spectrum.

The *N* region is characterized by broader emission lines (FWHM in the range ~850–1070 km s$^{-1}$ for Ly$\alpha$) and the gas is redshifted relative to the continuum centroid ($V_{\rm offset}$ in the range $\sim +50$ to $+250$ km s$^{-1}$). The C IV FWHM is $1220 \pm 40$ km s$^{-1}$. He II is too noisy in the VIMOS spectrum to measure its FWHM. However, Keck long-slit spectroscopy (Humphrey 2004) of this region implies FWHM $= 1100 \pm 100$ km s$^{-1}$. Therefore, the three lines in the north region are very broad compared with the south region.

Although absorption plays an important role in the Ly$\alpha$ spectral differences across the nebula (see below), kinematics are also clearly having an effect, since the C IV and He II lines show marked differences between the north and south regions.

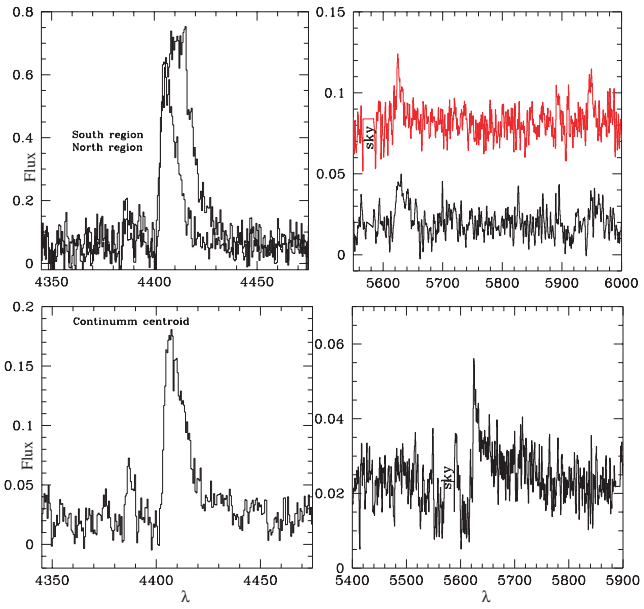


**Figure 7.** MRC 2025–218. Top: comparison between the Ly$\alpha$ (left-hand side) and C IV-He II (right-hand side) spectra from the northern and southern regions (see text). The southern C IV–He II spectrum has been shifted artificially in the flux scale for clarity. The two lines are detected in both regions. Bottom: Ly$\alpha$ (left-hand side) and C IV (right-hand side) spectra at the position of the continuum centroid. Note the very broad wings of both lines, signature of the broad-line region and the absorption features. In spite of the clear difference in FWHM, the shift in $\lambda$ of the Ly$\alpha$ line and the spatial separation between the two regions, note the exact coincidence in wavelength of the sharp edge in the blue wing of the line for the three spectra. Fluxes are in units of $10^{-16}$ erg s$^{-1}$ cm$^{-2}$ Å$^{-1}$.

The Ly$\alpha$ and C IV spectra at the position of the continuum centroid are shown in Fig. 7 (bottom panels). Very broad wings (presumably from the BLR; see Section 4.2) are seen in the line profiles of both Ly$\alpha$ and C IV.

*Ly$\alpha$ and C IV absorption*

The Ly$\alpha$ and C IV lines are clearly absorbed in this object (Fig. 7) as was already discussed by other authors (Villar-Martín et al. 1999). Since this paper is mostly focused on the properties of the emission-line nebulae, we will present here a general description and defer a more detailed analysis of the absorbers for another publication (Humphrey et al., in preparation).

Some peculiar properties of the Ly$\alpha$ spectral profile are a consequence of absorption rather than kinematics: the multiple peaks, the fact that the flux drops below the continuum level at some wavelengths, the sharp, almost vertical edge of the blue wing of the line and the identical wavelength over the nebula at which this sharp edge is measured (see below) are most naturally explained by absorption. Several absorption features are detected in both Ly$\alpha$ and C IV (Fig. 7).

Ly$\alpha$ absorption is detected in more than 30 spaxels. We set a lower limit to the size of the main absorber of $\sim$4.7 $\times$ 3.5 arcsec$^2$ or $\sim$43 $\times$ 32 kpc$^2$. It is possible that this absorber covers the Ly$\alpha$ nebula completely. Since absorption is detected in C IV as well, this implies that the absorbing gas is highly ionized.

A striking characteristic is that the sharp edge of the Ly$\alpha$ blue wing (see Fig. 7) happens at almost exactly the same wavelength (4403.3 $\pm$ 0.5 Å) in all spaxels where we have been able to measure it ($\sim$20), revealing very little kinematic structure of the main absorber along the LOS and across its whole spatial extension.

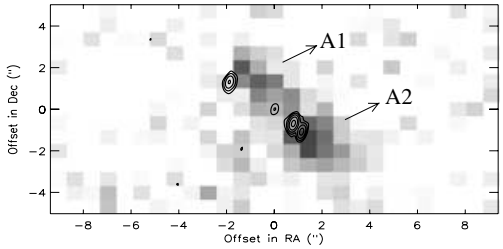


**Figure 8.** Ly$\alpha$ nebula associated with MRC 0140–257 with 8.2 GHz radio contours overlaid. Two main Ly$\alpha$ spatial components (*A*1 and *A*2) are identified in the image very closely aligned with the radio structures. The size of the nebula is $\sim$9 arcsec or 83 kpc. North is towards up and east towards left.

### 4.3 MRC 0140–257 ($z = 2.64$)

*The Ly$\alpha$ nebula*

The VIMOS Ly$\alpha$+continuum image of MRC 0140–257 was created by adding the monochromatic images of the object within the [4410–4430] Å range. An adjacent continuum image was subtracted to keep the line emission only. The resulting Ly$\alpha$ image is shown in Fig. 8 with the VLA 8.2 GHz radio contours overlaid (Carilli et al. 1997).

Two main spatial components (*A*1 and *A*2 in the figure) are identified in the image, which are aligned with the radio structures within a few degrees. We have assumed that the radio core is located between *A*1 and *A*2 (but see Section 2). The Ly$\alpha$ spatial centroids of *A*1 and *A*2 are separated by $\sim$3.5 arcsec or 32 kpc. The maximum extension of the nebula (*A*1 and *A*2) is 9 arcsec or 83 kpc. It therefore extends well beyond the radio structures. This conclusion is independent of the location of the radio core along the *A*1–*A*2 line (Section 2). The faintest Ly$\alpha$ emission we detect on the VIMOS data has surface brightness $\sim 10^{-17}$ erg s$^{-1}$ cm$^{-2}$ arcsec$^{-2}$ ($3\sigma$ values).

The total Ly$\alpha$ flux integrated over the nebula is $3.6 \times 10^{-16}$ erg s$^{-1}$ cm$^{-2}$, which, taking aperture corrections into account, is consistent with McCarthy et al. (1991a). It corresponds to a luminosity of $2.9 \times 10^{43}$ erg s$^{-1}$.

*Continuum morphology*

A continuum image was created by collapsing the data cube across the continuum spectral windows [5270–5550] and [5700–5800] Å, i.e. rest-frame range $\sim$[1450–1525] and [1565–1595] Å, respectively. For comparison, the optical image of McCarthy et al. (1992) was obtained using a Gunn–Thuan filter, covering the rest-frame range [1675–1920].[1] We detect a faint source, which overlaps partially with Component *A*1 (Fig. 9). Although the source is apparently extended in the N–S direction, this is dubious. The faintest structures to the north are consistent within the errors with the image detection limit. On the other hand, there are noise residuals at similar flux levels at different positions across the VIMOS FOV.

*Spatially extended emission-line spectroscopy*

We show in Fig. 10 the spatial maps of the FWHM and $V_{\rm offset}$ of the Ly$\alpha$ line. $V_{\rm offset}$ has been measured relative to the Ly$\alpha$

[1] The authors used a 2.5-m telescope and an exposure time of 2700 s to obtain this image.

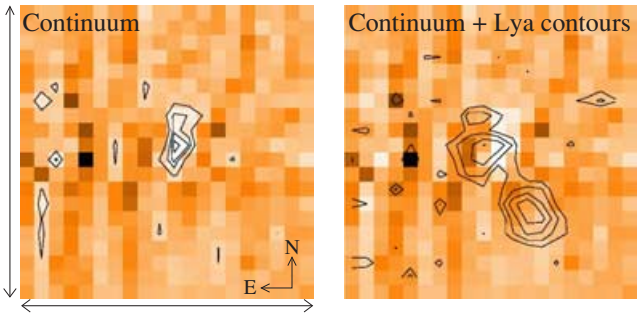


**Figure 9.** MRC 0140–257: comparison between the continuum and Ly$\alpha$ spatial distributions. Left-hand side: continuum images. Right-hand side: with Ly$\alpha$ contours overlaid. Ly$\alpha$ contours: (0.2, 0.4, 0.6, 1.0) $\times 10^{-16}$ erg s$^{-1}$ cm$^{-2}$ arcsec$^{-2}$. Continuum contours: (2.1,3.5,4.2,4.9) $\times 10^{-16}$ erg s$^{-1}$ cm$^{-2}$ arcsec$^{-2}$.

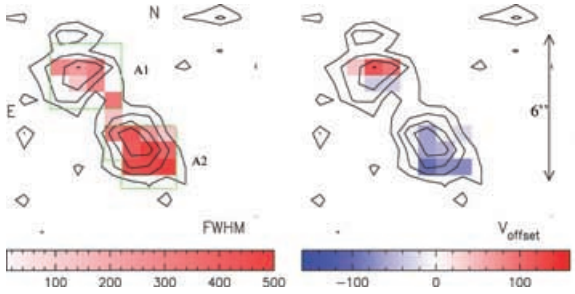


**Figure 10.** MRC 0140–257: Ly$\alpha$ spectral properties. The FWHM (left-hand side) (corrected for instrumental broadening) and the velocity shift (right-hand side) relative to the line emission at the intermediate spatial position between *A*1 and *A*2 are shown. Values are in km s$^{-1}$. Only coloured (i.e. not white) spaxels in the FWHM map have measured FWHM values. $V_{\rm offset}$ is shown for the same spaxels, with white corresponding in this case to 0 velocity. Ly$\alpha$ flux contours are overplotted. The apertures selected to extract the spectra of Components *A*1 and *A*2 (see text) are shown with green lines.

emission between *A*1 and *A*2. The errors on $V_{\rm offset}$ are estimated to be $<$40 km s$^{-1}$. The errors on the FWHM are in the range of 60–100 km s$^{-1}$. The main reason for these large relative errors is the uncertainty on the continuum level, due to the noise (this object is fainter) and the presence of an underlying broad component (see below). The line is narrow, with FWHM$\lesssim$500 km s$^{-1}$ across the whole nebula, compared with typical values of HzRG.

The Ly$\alpha$ spectra integrated over the highest signal-to-noise spaxels of *A*1 (16 spaxels) and *A*2 (14 spaxels, see Fig. 10, green lines) are shown in Fig. 11 (right-hand panels). In both spatial components, the Ly$\alpha$ spectral profile is dominated by a strikingly narrow component, with FWHM $= 250 \pm 50$ and $\lesssim$120 km s$^{-1}$ for *A*1 and *A*2, respectively. An underlying broad component seems to be also present in both components.[2] This is most clearly detected when both spectra are added. The fit to the line profile in the co-added spectrum of *A*1 and *A*2 is shown in Fig. 12 together with the individual components isolated in the fit. The underlying broad component has FWHM $=$ $1200 \pm 200$ km s$^{-1}$. The velocity shift between *A*1 and *A*2 is $120 \pm 20$ km s$^{-1}$, which is also rather low compared with typical values in HzRG (e.g. McCarthy et al. 1996a).

[2] Using a single Gaussian, as the fits used to produce Fig. 11 (left-hand panel) the narrow peak is broadened because of the broad wings and the derived FWHM have values of up to ∼500 km s$^{-1}$.

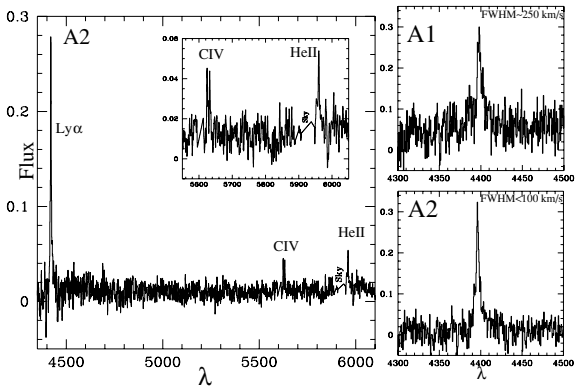


**Figure 11.** MRC 0140–257: spectra of *A*1 and *A*2. The Ly$\alpha$ spectral region is amplified in the right-hand panels. The complete spectrum is shown for *A*2 (left-hand panel) to highlight the detection of C IV and He II (small box). All lines are characterized by a very narrow component of FWM $<$ 300 km s$^{-1}$. The lines are unusually narrow for a high-redshift radio galaxy. Note that the C IV doublet is resolved. Flux is in units of $10^{-16}$ erg s$^{-1}$ cm$^{-2}$ Å$^{-1}$.

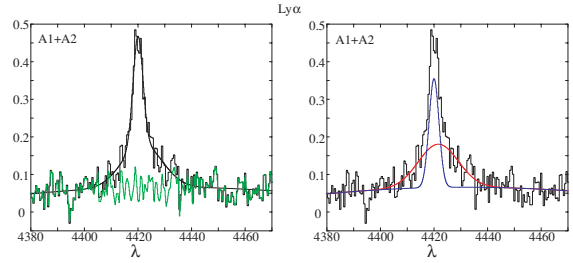


**Figure 12.** MRC 0140–257: Ly$\alpha$ spectrum of the co-added spectra of *A*1 and *A*2. The original data are shown with the best fit (thin solid line) and the residuals (green). The individual kinematic components (blue and red) are shown in the right-hand panels. A strikingly narrow component of FWHM $= 270 \pm 40$ km s$^{-1}$ is isolated on the top of an underlying broad component with FWHM $= 1200 \pm 200$ km s$^{-1}$. Flux is in units of $10^{-16}$ erg s$^{-1}$ cm$^{-2}$ Å$^{-1}$.

C IV and He II are detected in *A*2 (Fig. 11, left-hand panel). Two very narrow emission lines are identified at the expected wavelengths of the C IV doublet. We have fitted the lines with no constraints applied. The resulting doublet consists of two emission lines separated by $8.0 \pm 1.0$ Å (consistent with the errors with the theoretical 9.2 Å at the redshift of the object) and with flux ratio of $\sim 1.0 \pm 0.2$, as expected in the optically thin case. Taking the errors into account, both lines are unresolved (observed FWHM $= 2.5 \pm 0.6$ and $2.4 \pm 0.7$ Å, respectively), with FWHM $\lesssim$ 100 km s$^{-1}$. This is in excellent agreement with the width of the Ly$\alpha$ narrow component. He II is also detected and is similarly narrow with FWHM $=$ $180 \pm 60$ km s$^{-1}$.

The small FWHM values of the C IV and He II lines confirm that Ly$\alpha$ is intrinsically very narrow (rather than absorbed).

### *Lyα absorption*

The Ly$\alpha$ spectral profile does not show clear evidence for absorption. This is further supported by the large Ly$\alpha$ ratios. In *A*2, Ly$\alpha$/He II and Ly$\alpha$/C IV are $14.0 \pm 1.5$ and $7.4 \pm 1$, respectively. These values are consistent with standard photoionization model predictions for the measured C IV/He II $= 1.8 \pm 0.3$ (Villar-Martín et al. 2007). Ly$\alpha$/He II and Ly$\alpha$/C IV are $\gtrsim$6 and $\gtrsim$5, respectively, for *A*1 and it

is not possible to say whether Ly$\alpha$ is absorbed. The values for the integrated spectrum are $\geqslant$15 and 9 $\pm$ 2, respectively, which for the measured C IV/He II $\gtrsim$ 1.5 do not imply absorption either. This is in contradiction with Eales & Rawlings (1996) (see Section 3.3).

## 5 DISCUSSION

### 5.1 Main properties of the Ly$\alpha$ nebulae

The three radio galaxies investigated here are associated with giant (>60 kpc) Ly$\alpha$ nebulae. This was already known for MRC 1558–003 and 2025–218, but not for MRC 0140–257. The total Ly$\alpha$ luminosities are $\sim$(0.3–3.4) $\times$ $10^{44}$ erg s$^{-1}$, within the range of typical values measured for HzRG.

The morphologies are varied. The nebula of one source has a centrally peaked, rounded appearance (MRC 1558–003). In the other two objects, it consists of two spatial components. This bimodal morphology could be a consequence of an obscuring dust structure (e.g. Knopp & Chambers 1997; Reuland et al. 2003). For MRC 2025–218, this is supported by the fact that the continuum centroid coincides with a minimum in the Ly$\alpha$ flux. Pentericci et al. (2001) also proposed the existence of a dust lane in MRC 0140–257 to explain the near-infrared continuum morphology.

The alignment between the Ly$\alpha$ nebulae and the radio structures is remarkable in MRC 2025–217 and 0140–257 ($\lesssim$10°). In MRC 1558–003, the nebula is misaligned by 30 $\pm$ 5°. Similar values have been measured for other HzRG radio galaxies (McCarthy et al. 1995).

Based on previous, deeper spectroscopic studies and this work, we conclude that, although the high surface brightness emission tends to be confined within the radio lobes, Ly$\alpha$ emission is also detected beyond the radio structures in the three objects studied here (see also Villar-Martín et al. 2003 for other examples).

In one case (MRC 1558–003), the new data reveal Ly$\alpha$ emission outside any plausible ionization cone and far from the radio structures (see Reuland et al. 2003; Villar-Martín et al. 2006, for other examples). Projection effects might be responsible, since this is a broad-line object and this is our favoured explanation (see Section 5.3). Alternatively, part of the Ly$\alpha$ emission might be resonantly scattered or powered by a mechanism not related to the active nucleus, such as young stars (Villar-Martín et al. 2007). Unfortunately, the data are not deep enough to check whether lines other than Ly$\alpha$ are emitted in these regions. Cooling radiation (Haiman, Spaans & Quataert 2000) is an interesting possibility often discussed in the subject of radio-quiet (e.g. Nilsson et al. 2006) and radio-loud Ly$\alpha$ nebulae. However, the Ly$\alpha$ surface brightness we measure in regions outside the reach of the ionization cones ($\gtrsim$$10^{-17}$ erg s$^{-1}$ cm$^{-2}$ arcsec$^{-2}$) is too high as compared with the model predictions (see Villar-Martín et al. 2003 for a more detailed discussion on this issue; see also Dijkstra, Haiman & Spaans 2006).

### 5.2 Interactions

Interactions between the radio structures (jet and radio lobes) and the ambient gas are known to have a profound impact on the kinematic properties of the giant nebulae associated with many HzRG (Section 1).

For the three objects studied here, this is obvious only in MRC 2025–218, in the northern region in particular, where the emission lines Ly$\alpha$, He II and C IV have FWHM $\gtrsim$ 1000 km s$^{-1}$ (Section 4.2). No evidence for jet–gas interactions is found in the southern region, where the radio structures present a sharp bend (see Fig. 4). If this has been caused by the collision of the radio structures with a dense gaseous region,[3] no clear signature has remained in the gas kinematic properties.

Ly$\alpha$ is also very broad across the MRC 1558–003 nebula. However, FWHM > 1000 km s$^{-1}$ values are measured also in distant regions from the radio structures. Since moreover He II is relatively narrow (450–650 km s$^{-1}$ across the nebula), we cannot discard that resonance scattering effects are responsible for broadening the Ly$\alpha$ spectral profile.

In MRC 0140–257, the nebular emission is dominated by quiescent gas (Section 4.3), i.e. not perturbed by the radio structures. We cannot tell whether the faint Ly$\alpha$ underlying broad component (FWHM = 1200 $\pm$ 200 km s$^{-1}$) is a consequence of jet–gas interactions or resonance scattering effects. In fact, the most interesting result for this object is the strikingly quiescent kinematics revealed by the bulk of the emission lines across the nebula (FWHM < 300 km s$^{-1}$ and $V_{\rm offset}$ $\sim$ 120 km s$^{-1}$). This characteristic is unique among HzRG. Similar relaxed kinematics are rather extreme also among low-$z$ radio galaxies, since only a few show such narrow linewidths, usually measured in extranuclear regions (e.g. Baum et al. 1990).

### 5.3 Are the nebulae infalling?

Humphrey et al. (2007) proposed that the extended *quiescent* ionized nebulae associated with numerous powerful radio galaxies at different redshifts are in the process of infall. These authors searched for correlations between several radio and optical/UV asymmetries, and found that (i) the quiescent ionized gas has its highest redshift on the side of the nucleus with the brightest and more polarized radio hotspot and that (ii) on the side where the Ly$\alpha$ emission is brightest relative to the other emission lines and continuum. They concluded that orientation effects, with the quiescent gas in infall towards the nucleus, are the most natural scenarios for explaining these correlations.

Our study of MRC 2104–242 based on integral field VIMOS data also suggested that the giant Ly$\alpha$ nebula associated with this object could be in the process of infall (Villar-Martín et al. 2006). However, due to the uncertainty on the spatial gas distribution, a rotational pattern could not be discarded. It was our later work (Humphrey et al. 2007) on a larger sample which allowed us to discard rotation and favour the infall interpretation.

We investigate next whether the morphological and kinematic properties of the nebulae studied here are consistent with infall.

*MRC 1558–003*

According to Humphrey et al. (2007), the giant nebula associated with MRC 1558–003 is infalling towards the centre. Here, we describe an infall model that can explain the observations quite well. An AGN sits in the centre of a halo of mass $M_{\rm tot} = 5 \times 10^{12}$ M$_\odot$. A dusty torus surrounding the AGN causes it to photoionize a biconical region of the surrounding gas. The opening angle of each cone is assumed to be $\phi = 90°$. The cone axis is not perfectly aligned with the LOS, but intersects it at an angle of $\sim$20°. Furthermore, the cones are rotated by $\sim$10° counterclockwise on the sky. In this scenario, one cone is pointing almost directly at the observer, while the other points in the opposite direction. Photoionization and subsequent recombination in the cones convert ionizing radiation emitted by the

[3] Since this is a broad-line object, projection effects might exaggerate the angle of the observed bend of the radio structures.

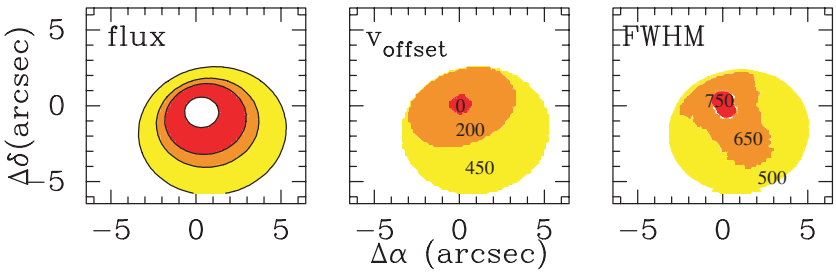


**Figure 13.** Observable properties of a model in which an AGN photoionizes a biconical region of the surrounding gas. One cone is pointing almost directly at the observer, while the other points in the opposite direction. The gas is collapsing on to the AGN (for model details, see Appendix A). If the Lyα flux from the cone that points away from the observer is not detected, then this model reproduces most observational features (except the Lyα FWHM) remarkably well. The left-hand panel shows the surface brightness profile. The contour levels are (0.03, 0.01.0.2 and 0.7) times the maximum surface brightness level. The central panel shows the redshift of the Lyα line with respect to that of the centroid (labels denote the offset in km $s^{-1}$). The right-hand panel shows the FWHM in km $s^{-1}$ of the Lyα line as a function of position.

AGN into Lyα, and thus result in spatially extended fluorescent Lyα emission (Haiman & Rees 2001). In this picture, infalling gas in the nearest cone will be emitted with a redshift relative to the systemic redshift.

We found that a model in which the gas density increases as $\rho \propto r^{-2}$, and the gas velocity increases $v(r) \propto r^{-1/2}$ can reproduce most observed properties of the nebula (Fig. 13). In order to match the observations, it is crucial that the emission from the furthest cone is not observed (see below). For a more detailed description of the model, the reader is referred to Appendix A. According to Fig. 13, our infall model produces the following features.

(i) A rounded and centrally peaked morphology (left-hand panel). This is a consequence of the geometry of our model and the increase of the recombination rate (and thus of fluorescent Lyα emission) towards the AGN. The innermost contour level in Fig. 13 encloses a surface brightness that is 25 times higher than that surrounded by the outermost contour. These properties are similar to those observed (Fig. 2) within a similar nebular size. In order to obtain a more symmetric appearance, as shown by the data, the axis cone should be closer to the LOS. This would correspond to a quasar. The fact that the AGN continuum and broad-line emission are detected at rest-frame optical wavelengths, but are not obvious in the UV rest frame, can be explained by the existence of dust obscuring the central regions.

(ii) The largest redshift is observed at the Lyα centroid (central panel), as observed in the data (Fig. 3, right-hand side). Because the infall velocity increases towards the AGN, the redshift of the Lyα line decreases outwards. Labels in the figure denote the mean velocity shift of the emission line in km $s^{-1}$ with respect to the centroid, i.e. the position of maximum Lyα flux. These values are consistent with the measured velocity offsets.

(iii) The nebular centroid has the largest redshift with respect to the systemic redshift. It is not possible to determine the systemic redshift in this object. However, it is interesting to note that in MRC 1558–003 Lyα is redshifted relative to the main rest-frame UV emission lines (C IV, He II, C III]) both in the spatially integrated spectrum (Röttgering et al. 1997) and at different spatial positions (Villar-Martín et al. 2003). In our scenario, the Lyα emission from the far cone is negligible. The other emission lines might also be fainter from the more distant cone because of extinction, but these effects would be less pronounced, since they are not affected by resonance scattering effects (see also Humphrey et al. 2007). As a result, the relative contribution from the far cone to the flux of these lines is larger than for Lyα both in the integrated spectrum and at different projected spatial positions. Since the emission from the more distant cone must be blueshifted relative to the near cone because of the infall pattern, the lines will be blueshifted relative to Lyα, which is consistent with the observations.

To reproduce these two last features, the Lyα emission detected from the furthest cone must be negligible as the expected blueshift of these photons would eliminate the predicted increase of the Lyα redshift towards the nebular centroid and the blueshift relative to other emission lines. Although radiation blueward of the rest-frame Lyα frequency is subject to absorption in the IGM, the IGM at $z = 2.6$ is not opaque enough to completely eliminate the flux from the far cone [we used the model of Dijkstra et al. (2007) to calculate the impact of the IGM on the Lyα line]. Alternatively, the flux from the far side could be eliminated by a neutral and dusty spatially extended structure that lies between the two cones. Several studies suggest the existence of such structure (e.g. van Ojik et al. 1997; Humphrey et al. 2006).

Our model has greater difficulty reproducing the observed Lyα FWHM (right-hand panel, Fig. 11). Especially if purely radial infall is considered, the model produces a maximum FWHM of ∼500 km $s^{-1}$, which is a factor of almost 3 short of what is observed for Lyα. The model FWHM that is shown in Fig. 11 is boosted to 750 km $s^{-1}$ by convolving the spectrum at each pixel with a Gaussian with a standard deviation of $\sigma_{1D} = v_{circ}/\sqrt{2} \sim 250\,km\,s^{-1}$ ($\sigma_{1D}$ is the 1D velocity dispersion of the halo). This reflects that the infall probably does not occur purely along radial paths. Although inconsistent with the Lyα measurements, this model successfully reproduces the spatial variation of the He II FWHM observed by (Villar-Martín et al. 2003) along the radio axis using long-slit spectroscopic data. In this direction, the nebula shows broader FWHM ∼ 750 km $s^{-1}$ at the spatial centroid and ∼500 km $s^{-1}$ in the outer parts (Villar-Martín et al. 2003), consistent with the models.

Resonant scattering of Lyα photons has been ignored in our model because the gas within the cones is highly ionized and likely optically thin to Lyα (see Appendix A). Although resonant scattering effects could explain the large Lyα FWHM values and its broader profile compared with He II (Section 4.1), they would contradict other observational results. Dijkstra et al. (2006) have performed radiative transfer calculations through neutral collapsing gas clouds and found that resonant scattering does not only broaden the Lyα line, but that energy transfer from the infalling gas to the Lyα photons shifts the line to bluer wavelengths. On the contrary, the observations suggest that the Lyα line is redshifted with respect to other emission lines and probably relative to the system's redshift.

Neither does resonant scattering through optically thick, collapsing gas clouds reproduce the observation that the Ly$\alpha$ line is redshifted more towards the centre. If resonant scattering does not occur, then it remains to be explained why Ly$\alpha$ shows such large FWHM values and it is much broader than He II.

An alternative mechanism that can broaden Ly$\alpha$ relative to other emission lines and could produce a similar velocity pattern as that of infall is outflows (Dijkstra et al. 2006). In this scenario, a shell propagates outwards from the centre, which is thick enough to be self-shielding (with column densities of hydrogen of $10^{20}$ cm$^{-2}$). All material is highly ionized, except inside the shell that is moving outwards. In this case, Ly$\alpha$ photons basically bounce off the shell as if it were a mirror, scattering back and forth between the two expanding mirrors until they have been Doppler boosted far enough for them to be able to simply propagate through the shell (each time a Ly$\alpha$ photon scatters off the shell, it picks up a Doppler shift from the shell). This process will broaden Ly$\alpha$, not affecting the other emission lines. Detailed modelling would be necessary to test whether outflows can reproduce all other observed properties of the nebula as infall does. However, since outflows cannot explain the radio/optical asymmetries seen in MRC 1558–003 (Humphrey et al. 2007), which, on the other hand, are successfully explained with infall, here we will not explore the outflow scenario further.

In conclusion, our infall model can successfully explain the morphology, size, surface brightness distribution and the velocity field of the Ly$\alpha$ nebula associated with MRC 1558–003. It can also explain why Ly$\alpha$ is redshifted relative to other emission lines and the FWHM values of the non-resonant He II line. The infall scenario is also consistent with our previous results which imply that the *quiescent* nebulae in many HzRG (and MRC 1558–003 in particular) are infalling (Humphrey et al. 2007). On the other hand, this model fails to explain the large Ly$\alpha$ FWHM values. A mechanism which might not be connected with the infall process could be responsible for the line broadening, while keeping the infall pattern and the He II FWHM intact.

*MRC 2025–218*

It is not possible to investigate the kinematic pattern of the quiescent gas, since the data do not allow us to isolate its emission in the north component.

*MRC 0140–257*

It is not possible to disentangle how the quiescent gas is moving in this object. The relaxed kinematics are not suggestive of outflows.

MRC 0140–257 does not follow the trend found by Humphrey et al. (2007) in powerful radio galaxies at different $z$, such that the quiescent gas has the highest redshift at the side of the brightest and more polarized radio hotspot. The authors interpret these results as evidence for infall. On the contrary, the highest redshift in MRC 0140–257 is measured in $A1$, at the side of the fainter (northern) radio hotspot.

This discrepancy could be due to three different reasons: (i) the orientation diagnostics based on the radio properties are not valid; (ii) the gas is not in infall and (iii) our radio-optical registration (Section 2) is incorrect. If the radio core was located on $A1$ or $A2$ (rather than between the two Ly$\alpha$ components), we would have no information on the redshift on one side of the nucleus.

The interpretation of infall by Humphrey et al. (2007) is based on the fact that the radio asymmetries in their sample provide a powerful diagnostic tool to constrain the orientation of the radio source (and the Ly$\alpha$ nebula as a consequence). One possible explanation for the MRC 0140–257 discrepancy is that in this particular case the radio properties are not reliable indicators of the object orientation. This is actually suggested by the fact that the brightest (southern) hotspot shows the lowest polarization (Carilli et al. 1997), contrary to what we would expect if both flux and polarization asymmetries were mostly determined by orientation.

The orientation diagnostics based on the radio properties would fail, for instance, when the radio axis is very close to the plane of the sky. For MRC 0140–257, on the contrary, the detection of a radio core (Carilli et al. 1997) rather suggests that the angle between the radio axis and the plane of the sky is not negligible.

The diagnostics would also fail if the radio asymmetries are a consequence of environmental effects (e.g. McCarthy, van Breugel & Kapahi 1991b), rather than orientation. This is possibly the case in MRC 0140–257. On one hand, the brightest, less polarized hotspot is closest to the nucleus, and the Ly$\alpha$ emission on that side of the nucleus (adopting our present radio-optical registration) is also brightest. This is what we expect from McCarthy et al. (1991b) environmental scenario. On the other hand, the southern (brighter) radio structure consists of two radio hotspots (Fig. 8). If this is due to interactions with the gas (e.g. Carilli et al. 1997), this process would enhance the radio emission and the higher brightness of the southern radio structure would therefore be a consequence of environmental effects.

Alternatively, it is possible that the Ly$\alpha$ nebula is not infalling towards the centre. $A1$ and $A2$ could be two objects rotating around a common centre of mass (e.g. De Breuck et al. 2005). If this is located between $A1$ and $A2$, we estimate a dynamical mass of $>3 \times 10^9$ M$_\odot$ for a radius $r = 16$ kpc and a projected rotation velocity of 60 km s$^{-1}$ (i.e. half of the $V_{\rm offset}$ value between $A1$ and $A2$). This mass value is at least a factor of 100 smaller than the stellar masses inferred for other HzRG (Villar-Martín et al. 2006; Seymour et al. 2007) or for massive, early-type galaxies at $z \sim 2$ in deep, IR surveys (e.g. Daddi et al. 2004). MRC 0140–257 could be an unusually small mass HzRG, a possibility that is also suggested by the small FWHM values measured in $A1$ and $A2$. It would be essential to obtain rest-frame $H$ and $K$ magnitudes (e.g. Villar-Martín et al. 2006; Seymour et al. 2007) to make a proper estimation of the stellar mass.

If, on the contrary, this is progenitor of a massive elliptical galaxy, as one expects for a powerful HzRG (e.g. McLure et al. 1999), the rotation plane of $A1$ and $A2$ must almost coincide with the plane of the sky.

### 5.4 Ly$\alpha$ absorption

Ly$\alpha$ absorption has definitively been detected in MRC 2025–218, spatially extended for $\gtrsim 43 \times 32$ kpc$^2$. The absorber could therefore be larger in size than the optical size of the host (if already formed) underlying galaxy. C IV is also absorbed and, thus, the absorbing gas is highly ionized. As in this object, very little kinematic structure along the LOS was also found by Wilman et al. (2005) across the giant Ly$\alpha$ radio-quiet nebula LAB-2 discovered by Steidel et al. (2000). A more detailed analysis of the absorbers associated with MRC 2025–218 will be presented in Humphrey et al. (in preparation).

## 6 SUMMARY AND CONCLUSIONS

The morphological and spectroscopic properties of the giant (>60 kpc) Ly$\alpha$ nebulae associated with three radio galaxies

(MRC 1558–003, 2025–218 and 0140–217) at $z \sim 2.5$ have been investigated using VIMOS integral field spectroscopic data on VLT. The three objects are associated with giant (>60 kpc) Ly$\alpha$ nebulae. This was already known for MRC 1558–003 and 2025–218, but not for MRC 0140–257.

The morphologies are varied. In one source, the nebula has a centrally peaked, rounded appearance (MRC 1558–003), while in the other two objects it consists of two spatial components (MRC 2025–218 and 0140–257). The total Ly$\alpha$ luminosities are in the range (0.3–3.4) $\times 10^{44}$ erg s$^{-1}$.

The Ly$\alpha$ spectral profile shows strong variation through the nebulae, with FWHM values in the range ∼400–1500 km s$^{-1}$ and velocity shifts $V_{\rm offset} \sim$ 120–600 km s$^{-1}$. Kinematic disturbance induced by the radio structures plays a clear important role in MRC 2025–218.

Most spectroscopic and morphological properties of the giant nebula associated with MRC 1558–003 are successfully explained by a scenario such that the giant nebula is collapsing towards the centre in the potential well of a $5 \times 10^{12}$ M$_\odot$ halo. This is consistent with our previous conclusion that the giant *quiescent* nebulae associated with this and other HzRG are in infall (Humphrey et al. 2007). On the other hand, this model has problems to reproduce the large Ly$\alpha$ FWHM values (>1000 km s$^{-1}$), which might be the consequence of a mechanism unrelated to the infall process.

We have discovered a giant (∼75 kpc) Ly$\alpha$ nebulae associated with a radio galaxy at $z$=2.64. It is very closely aligned with the radio axis and it extends well beyond the radio structures. It is characterized by a strikingly relaxed kinematics (FWHM < 300 km s$^{-1}$ and $V_{\rm offset} \lesssim 120$ km s$^{-1}$), unique among HzRG. This object might have an unusually small dynamical mass ($\gtrsim 3 \times 10^9$ M$_\odot$) for a HzRG, although this needs further investigation with other type of data.

Ly$\alpha$ absorption is definitively detected in MRC 2025–218. The absorbing screen has a spatial extension of $43 \times 32$ kpc$^2$ at least. It is highly ionized (C IV is also absorbed) and shows a remarkable velocity coherence (<100 km s$^{-1}$) across its spatial extension.

## ACKNOWLEDGMENTS

Thanks to an anonymous referee for useful comments on the paper. We thank Chris Carilli and Laura Pentericci for providing the radio maps presented in this paper. The work of MVM and RGD has been supported by the Spanish Ministerio de Educación y Ciencia and the Junta de Andalucía through the grants AYA2004-02703 and TIC-114. SFS thanks the Spanish Plan Nacional de Astronomía, program AYA2005-09413-C02-02 (MEC) and the Plan Andaluz de Investigación of Junta de Andalucía, research group FQM322. AH acknowledges the support from a UNAM postdoctoral research fellowship. Thanks to Joel Vernet for producing Figs 3 and 8.

## REFERENCES

Barthel P., 1989, ApJ, 336, 606
Baum S., Heckman T., van Breugel W., 1990, ApJS, 74, 389
Carilli C., Röttgering H., van Ojik R., Miley G., van Breugel W., 1997, ApJSS, 109, 1
Daddi E. et al., 2004, ApJ, 600, L127
De Breuck C., van Breugel W. J. M., Stanford S. A., Röttgering H., Miley G., Stern D., 2002, AJ, 123, 637
De Breuck C., Downes D., Neri R., van Breugel W., Reuland M., Omont A., Ivison R., 2005, A&A, 430, L1
Dijkstra M., Haiman Z., Spaans M., 2006, ApJ, 649, 14
Dijkstra M., Lidz A., Wyithe S., MNRAS, 2007, 377, 1175
Eales S., Rawlings S., 1996, ApJ, 460, 68
Eales S., Rawlings S., Dickinson M., Spinrad H., Hill G., Lacy M., 1993, ApJ, 409, 578
Haiman Z., Rees M. J., 2001, ApJ, 556, 87
Haiman Z., Spaans M., Quataert E., 2000, ApJ, 537, L5
Humphrey A., 2004, PhD thesis, Univ. Hertfordshire
Humphrey A., Villar-Martín M., Fosbury R.Vernet J., di Serego Alighieri S., 2006, MNRAS, 369, 1103
Humphrey A., Villar-Martín M., Fosbury R.Vernet J., di Serego Alighieri S., 2007, MNRAS, 375, 705
Knopp G., Chambers K., 1997, ApJS, 109, 367
Kurk J., Pentericci L., Röttgering H M. G., 2002, Revista Mexicana de Astronomía y Astrofísica (Serie de Conferencias), 13, 191
Large M., Mills B., Little A., Crawford D., Sutton J., 1981, MNRAS, 194, 693
Larkin J. et al., 2000, ApJ, 533, L61
Le Févre O. et al., 2003, in Masanori I., Moorwood A. F., eds, Proc. SPIE 4841, p. 1670
Maxfield L., Spinrad H., Stern D., Dey A., Dickinson M., 2002, AJ, 123, 2321
McCarthy P., 1993, ARA&A, 31, 639
McCarthy P. J., Spinrad H., Dickinson M., van Breugel W., Liebert J., Djorgovski S., Eisenhardt P., 1990a, ApJ, 365, 487
McCarthy P. J., Kapahi V., van Breugel W., Subrahmanya C., 1990b, AJ, 100, 1014
McCarthy P. J., van Breugel W., Kapahi V., Subrahmanya C., 1991a, AJ, 102, 522
McCarthy P. J., van Breugel W., Kapahi V., 1991b, ApJ, 371, 478
McCarthy P., Persson S., West S., 1992, ApJ, 382, 52
McCarthy P. J., Spinrad H., van Breugel W., 1995, ApJS, 99, 27
McCarthy P., Baum S., Spinrad H., 1996a, ApJS, 106, 281
McLure R., Kukula M., Dunlop J., Baum S., O'Dea C., Hughes D., 1999, MNRAS, 308, 377
Nilsson K., Fynbo J., Möller P., Sommer-Larsen J., Ledoux C., 2006, A&A, 452, L23
Pentericci L., Röttgering H., Miley G., McCarthy P., Spinrad H., van Breugel W., Macchetto F., 1999, A&A, 341, 329
Pentericci L., Van Reeven W., Carilli C., Röttgering H., Miley G., 2000, A&AS, 145, 121
Pentericci L., McCarthy P., Röttgering H., Miley G., van Breugel W., Fosbury R., 2001, ApJS, 135, 63
Reuland M. et al., 2003, ApJ, 592, 755
Reuland M. et al., 2007, AJ, 133, 2607
Röttgering H., van Ojik R., Miley G., Chambers K., van Breugel W., de Koff S., 1997, A&A, 326, 505
Sánchez S. F., 2004, AN, 325, 167
Sánchez S. F., 2006, AN, 327, 850
Sandage A., Tamman G., Saha A., Reindl B., Macchetto F., Panagia N., 2006, ApJ, 653, 843
Seymour N. et al., 2007, ApJS, in press (astro-ph/0703224)
Steidel C., Adelberer K., Shapley A., Pettini M., Dickinson M., Giavalisco M., 2000, ApJ, 532, 170
Tadhunter C., Fosbury R., Quinn P., 1989, MNRAS, 240, 225
Van Ojik R., Röttgering H., Carilli C., Miley G., Bremer M., Macchetto F., 1996, A&A, 313, 25
Van Ojik R., Röttgering H., Miley G., Hunstead R., 1997, A&A, 317, 358
Vernet J., Fosbury R., Villar-Martín M., Cohen M., Cimatti A., di Serego Alighieri G. R., 2001, A&A, 366, 7
Villar-Martín M., Fosbury R., Binette L., Tadhunter C., Rocca-Volmerange B., 1999, MNRAS, 351, 47
Villar-Martín M., Vernet J., di Serego Alighieri S., Fosbury R., Humphrey A., Pentericci L., 2003, MNRAS, 346, 273
Villar-Martín M. et al., 2006, MNRAS, 359, 5
Villar-Martín M., Humphrey A., De Breuck C., Fosbury R., Binette L., Vernet J., 2007, MNRAS, 375, 1299
Wilman R., Gerssen J., Bower R., Morris R., Bacon R., de Zeeuw P., Davies R., 2005, Nat, 436, 227

## APPENDIX A: INFALL MODEL OF MRC 1558–003

For each position ($\alpha$, $\delta$), the spectrum was obtained by adding the emission from each cell ($\alpha$, $\delta$, $z$) inside the cone along that LOS. The emissivity for a cell was calculated by assuming photoionization equilibrium. This implies the volume emissivity at radius $r$ scales as $\epsilon(r) \propto n_{\rm H}^2(r)$, where $n_{\rm H}(r)$ is the number density of hydrogen nuclei at radius $r$, and we used that the gas is (almost) fully ionized.

In the frame of the cell (which itself is falling towards the centre), the Ly$\alpha$ line is broadened by thermal motions of the atoms in the gas, which results in a Voigt profile. The bulk motions of the cell then cause a Doppler shift of the Ly$\alpha$ line. The total spectrum at ($\alpha$, $\delta$) on the sky, denoted by $S(\alpha, \delta, x)$, is obtained by adding the contributions from all cells. To be more precise, the spectrum at ($\alpha$, $\delta$) is given by

$$S(\alpha, \delta, x) \propto \int {\rm d}s\, \epsilon(\alpha, \delta, s)\, \phi\left[x - \frac{v(s)}{v_{\rm th}}\right], \tag{A1}$$

where $\epsilon(\alpha, \delta, s) = n_{\rm H}^2\ (\alpha, \delta, s)$ if the cell is inside the cone, and otherwise $\epsilon(\alpha, \delta, s) = 0$. Furthermore, $\phi(x)$ is the Voigt function.[4]

The gas density and velocity profiles were assumed to be of the forms $n_{\rm H}(r) \propto r^{-2}$, $v(r) \propto r^{-1/2}$. The infall velocity was assumed to be equal to the circular velocity of the halo at the virial radius to prevent both fields from diverging, both $n_{\rm H}$ and $v$ were kept constant at radii less than 0.15 times the virial radius (which corresponds to $0.15 \times 160 = 24$kpc). These fields were chosen to give the best agreement with the observations. Note that these parameters were chosen to produce a good fit to the observations. To enhance the FWHM at each location ($\alpha$, $\delta$) were convolved with a Gaussian of width $\sigma_{\rm 1D} = v_{\rm circ}/\sqrt{2} \sim 250\,{\rm km\ s^{-1}}$.

Equation (A1) is valid in the limit where the cloud is transparent to all Ly$\alpha$ photons. In our model, the Ly$\alpha$ from the furthest cone is not observed and we only need to consider Ly$\alpha$ emission from the nearest cone. For these photons, we find that the optically thin approximation is very reasonable: all Ly$\alpha$ photons are emitted in the cone where the gas is highly ionized. For the cone orientation of our model, each Ly$\alpha$ photon never leaves the cone on its way to the observer. The total optical depth for a given Ly$\alpha$ photon is reduced even further by velocity gradients along a LOS. Since all these photons are emitted predominantly redwards of the Ly$\alpha$ resonance, scattering in the IGM is not important.

[4] The Voigt function is given by $\phi(x) = \frac{a}{\pi}\int_{-\infty}^{\infty} \frac{e^{-y^2}dy}{(y-x)^2+a^2}$, where $a = A_{21}/4\pi\Delta\nu_D = 4.7 \times 10^{-4}(13\ {\rm km\ s^{-1}}/v_{\rm th})$. Here $A_{21}$ is the Einstein A coefficient for the transition, $v_{\rm th}$ is the thermal velocity of the hydrogen atoms in the gas, given by $v_{\rm th} = \sqrt{2k_{\rm B}T/m_{\rm p}}$, where $k_{\rm B}$ is the Boltzmann constant, $T$ the gas temperature and $m_{\rm p}$ the proton mass.

This paper has been typeset from a TEX/LATEX file prepared by the author.